Supplemental Material can be found at:
http://www.jbc.org/cgi/content/full/M807947200/DC1

THE JOURNAL OF BIOLOGICAL CHEMISTRY VOL. 284, NO. 12, pp. 7646–7655, March 20, 2009
© 2009 by The American Society for Biochemistry and Molecular Biology, Inc. Printed in the U.S.A.

Structural Basis of Inhibition Specificities of 3C and 3C-like Proteases by Zinc-coordinating and Peptidomimetic Compounds*[S]

Received for publication, October 16, 2008, and in revised form, December 26, 2008 Published, JBC Papers in Press, January 14, 2009, DOI 10.1074/jbc.M807947200

Cheng-Chung Lee[‡§¶1], Chih-Jung Kuo[§‖1], Tzu-Ping Ko[§¶], Min-Feng Hsu[§¶], Yao-Chen Tsui[§], Shih-Cheng Chang[‡‡§§], Syaulan Yang[¶¶], Shu-Jen Chen[¶¶], Hua-Chien Chen[¶¶], Ming-Chu Hsu[¶¶], Shin-Ru Shih[‡‡§§], Po-Huang Liang[§¶‖**2], and Andrew H.-J. Wang[‡§¶‖**3]**

*From the [‡]Structural Biology Program, Institute of Biochemistry and Molecular Biology, National Yang-Ming University, Taipei 11221, Taiwan, [§]Institute of Biological Chemistry, [¶]National Core Facility of High-Throughput Protein Crystallography, and [‖]Taiwan International Graduate Program, Academia Sinica, Taipei 11529, Taiwan, **Institute of Biochemical Sciences, National Taiwan University, Taipei 10617, Taiwan, [‡‡]Department of Medical Biotechnology and Laboratory Science, Chang Gung University, and [§§]Clinical Virology Laboratory, Department of Clinical Pathology, Chang Gung Memorial Hospital, Tao-Yuan 333, Taiwan, and [¶¶]TaiGen Biotechnology, Taipei 114, Taiwan*

Human coxsackievirus (CV) belongs to the picornavirus family, which consists of over 200 medically relevant viruses. In picornavirus, a chymotrypsin-like protease ($3C^{pro}$) is required for viral replication by processing the polyproteins, and thus it is regarded as an antiviral drug target. A 3C-like protease ($3CL^{pro}$) also exists in human coronaviruses (CoV) such as 229E and the one causing severe acute respiratory syndrome (SARS). To combat SARS, we previously had developed peptidomimetic and zinc-coordinating inhibitors of $3CL^{pro}$. As shown in the present study, some of these compounds were also found to be active against $3C^{pro}$ of CV strain B3 (CVB3). Several crystal structures of $3C^{pro}$ from CVB3 and $3CL^{pro}$ from CoV-229E and SARS-CoV in complex with the inhibitors were solved. The zinc-coordinating inhibitor is tetrahedrally coordinated to the His^{40}-Cys^{147} catalytic dyad of CVB3 $3C^{pro}$. The presence of specific binding pockets for the residues of peptidomimetic inhibitors explains the binding specificity. Our results provide a structural basis for inhibitor optimization and development of potential drugs for antiviral therapies.

Coxsackieviruses (CVs)[4] are positive sense, single-stranded RNA viruses, which belong to the Picornaviridae family (1). Symptoms of infection with CV B-group include fever, headache, sore throat, gastrointestinal distress, as well as chest and muscle pain, known as pleurodynia or Bornholme disease in many areas. In some cases, the symptoms progress to myocarditis or pericarditis, which can result in permanent heart damage or death. Coxsackie B virus infection may also induce aseptic meningitis. As a group, CV are the most common cause of unexpected sudden death and may account for up to 50% of such cases (2). The various members of the coxsackievirus B-group were discovered almost entirely in the United States, although a sixth member of the group has been found in the Philippines (1).

To date, no specific therapy for diseases caused by picornaviruses is available, although some general purpose antiviral drugs are in use. In Picornaviridae, a virally encoded chymotrypsin-like protease ($3C^{pro}$) is required for the proteolytic processing of the large polyproteins translated from the viral RNA genomes and thus is essential for viral replication (1, 3). The $3C^{pro}$ in rhinovirus (RV), another member of the Picornaviridae family, has been used as a drug target to develop the peptidomimetic inhibitor AG7088, aiming for treatment of the common cold. This inhibitor contains a lactam ring to mimic Gln at the P1 position and an α,β-unsaturated ester at P1′ as a Michael acceptor to form a covalent bond with the active site Cys residue (4–6).

Analogous to picornaviruses, human coronaviruses (CoV) are also positive sense, single-stranded RNA viruses, which contain a 3C-like protease ($3CL^{pro}$) for viral polyprotein processing. The virus of severe acute respiratory syndrome (SARS), which caused an outbreak in 2002–2003 that killed ~800 patients, has been identified as a human CoV, named SARS-CoV (7–10). The other members of CoV include CoV-229E, CoV-OC43, CoV-HKU, and CoV-NL63 (11–13). Although sharing similar substrate specificity with $3C^{pro}$ in recognizing

* This work was supported by grants from Academia Sinica and the National Science Council, Taiwan (NSC-95-3112-B-001-015-Y to A. H.-J. W.) for the National Core Facility of High-Throughput Protein Crystallography at Academia Sinica, Taiwan. The costs of publication of this article were defrayed in part by the payment of page charges. This article must therefore be hereby marked "*advertisement*" in accordance with 18 U.S.C. Section 1734 solely to indicate this fact.

[S] The on-line version of this article (available at http://www.jbc.org) contains supplemental Figs. S1 and S2.

The atomic coordinates and structure factors (codes 2ZTZ, 2ZU1, 2ZTY, 2ZTX, 2ZU2, 2ZU3, 2ZU4, and 2ZU5) have been deposited in the Protein Data Bank, Research Collaboratory for Structural Bioinformatics, Rutgers University, New Brunswick, NJ (http://www.rcsb.org/).

[1] Both authors contributed equally to this work.

[2] To whom correspondence may be addressed. Tel.: 886-2-2785-5696, ext. 6070; Fax: 886-2-2788-9759; E-mail: phliang@gate.sinica.edu.tw.

[3] To whom correspondence may be addressed. Tel.: 886-2-2788-1981; Fax: 886-2-2788-2043; E-mail: ahjwang@gate.sinica.edu.tw.

[4] The abbreviations used are: CV, coxsackievirus; $3C^{pro}$, 3C protease; RV, rhinovirus; $3CL^{pro}$, 3CL protease; CoV, coronavirus; SARS, severe acute respiratory syndrome; EPDTC, *N*-ethyl-*N*-phenyldithiocarbamate; Dabcyl, 4-(4-dimethylaminophenylazo)benzoic acid; Edans, 5-[(2-aminoethyl)amino]naphthalene-1-sulfonic acid; MES, 2-(*N*-morpholino)ethanesulfonic acid; MPD, methyl-2,4-pentanediol; HPLC, high pressure liquid chromatography; DMSO, dimethyl sulfoxide; PEG, polyethylene glycol; RT, reverse transcription.

Downloaded from www.jbc.org at National Taiwan Univ Medical Library on June 10, 2009

Gln as the P1 residue (14), the 3CL^{pro} of SARS-CoV possess no sequence homology with those of the 3C^{pro} type. AG7088, a potent inhibitor of RV 3C^{pro}, was tried but failed to inhibit 3CL^{pro} of SARS-CoV (15), indicating subtle structural differences in their active sites. However, AG7088 analogues and several classes of novel inhibitors have been discovered to combat SARS-CoV by targeting its 3CL^{pro} (16, 17).

In an attempt to develop new inhibitors against CV, in this study we have prepared, characterized, and solved the crystal structure of the recombinant 3C^{pro} from CVB3. Two classes of SARS-CoV 3CL^{pro} inhibitors, zinc-coordinating and peptidomimetic compounds (18–20), were tested and found active against the recombinant 3C^{pro} of CVB3. We also determined the structures of 3C^{pro} and 3CL^{pro} complexes with these inhibitors to elucidate the binding specificity. Our results could serve as the structural basis for further inhibitor optimization and development of potential drugs for antiviral therapies.

EXPERIMENTAL PROCEDURES

Preparation of SARS-CoV 3CL^{pro}, CoV-229E 3CL^{pro}, and CVB3 3C^{pro}—SARS-CoV 3CL^{pro} was prepared as described previously (21). The gene encoding CoV-229E 3CL^{pro} was cloned from viral cDNA obtained from Tri-Service General Hospital (Taipei, Taiwan) using PCR. Primers (forward, 5′-CGCGGATCCATCGAAGGTCGTGCTGGTTTGCGCAAAATGGCAC-3′ (encoding Factor Xa cleavage site); and reverse, (5′-CCGCTCGAGTCATTGCAGGTTAACACCAAACATTTGTTTG-3′) containing BamHI and XhoI restriction sites (underlined) were used. The PCR product was digested by BamHI and XhoI and then ligated into pGEX-6p-1 vector (GE Healthcare), which contains a glutathione *S*-transferase tag at the N terminus.

The gene encoding CVB 3C^{pro} was cloned from viral cDNA obtained from Chang-Gung Memorial Hospital (Tao-Yuan, Taiwan) by PCR. Primers (forward, 5′-CATGCCATGGGCCCTGCCTTTGAGTT-3′; and reverse, 5′-GCGCTCGAGTCAATGATGATGATGATGATGTTGCTCATCATTGAAGTAGTG-3′) containing NcoI and XhoI restriction sites (underlined) were used for C-terminal His_6 tag construction. The PCR products were digested with NcoI and XhoI, and the DNA fragment were cloned into pET16b (Novagen). The correct constructs were subsequently transformed to *Escherichia coli* BL21 (Novagen) for protein expression. Overnight culture (5 ml) of a single transformation was used to inoculate 500 ml of fresh LB medium containing 100 μg/ml ampicillin. The cells were grown to $A_{600} = 0.6$ and induced with 1 mM isopropyl-β-thiogalactopyranoside at 20 °C. After 16 h, the cells were harvested by centrifugation at 7000 × *g* for 15 min.

Purification of the proteases was conducted at 4 °C. His-tagged CVB3 3C^{pro} was purified using a nickel-nitrilotriacetic acid column and eluted with 25 mM Tris-HCl, pH 7.5, 120 mM NaCl, and 300 mM imidazole. The protein solution was dialyzed against 2× 2L buffer (containing 12 mM Tris-HCl, pH 7.5, 120 mM NaCl, and 0.1 mM EDTA, 7.5 mM β-mercaptoethanol, and 1 mM dithiothreitol). The 229E 3CL^{pro} was purified using a glutathione *S*-transferase column and then treated with Factor Xa to remove the fusion tag. For further purity improvement and buffer exchange of both enzymes, a HiTrap™ 26/10 QFF column (GE Healthcare) was used with the buffers, which contained 50 mM Tris-HCl, pH 7.5, 1 mM EDTA, and 1 mM dithiothreitol (for CVB3 3C^{pro}) and 1 M NaCl and 50 mM Tris-HCl, pH 8.0 (for 229E 3CL^{pro}). The purified proteins were concentrated for crystallization.

Peptide Synthesis and Examination of Substrate Specificity—The peptides used for testing as protease substrates were synthesized by using a 433A peptide synthesizer (Applied Biosystems). Starting with 0.10 mmol (0.101 g) of *p*-hydroxymethylphenoxymethyl polystyrene resin (1.01 mmol/g), synthesis was performed using a stepwise FastMoc protocol (Applied Biosystems). The amino acids were introduced using the manufacturer's prepacked cartridges (1 mmol each). Mass spectra of the synthesized peptides were obtained using the Finnigan LCQ mass spectrometer with an electrospray ion source.

For examining the substrate specificity of the protease, each peptide at 50 μM was incubated with 1 μM protease for 12 h, and the resulting mixture was analyzed by C-18 reverse-phase HPLC using the above mentioned conditions. The peak areas of the product were integrated to calculate the reaction rate of each peptide substrate under catalysis of the protease. The optimal peptide substrate was labeled with a fluorescence quenching pair; thereby the fluorogenic peptide (Dabcyl-KTSAVLQSGFRKME-Edans) could be used to measure the protease activity.

Protease Activity Assays—By using the fluorogenic peptide, the kinetic measurements were performed in 10 mM MES (pH 6.5, the optimal pH for protease activity) at 25 °C. Enhanced fluorescence due to cleavage of the peptide was monitored at 538 nm with excitation at 355 nm using a fluorescence plate reader (Fluoroskan Ascent, Thermo Scientific). The enzyme concentration used in measuring K_m and k_{cat} values was 0.5 μM, and the substrate concentrations were 0.5–5-fold the K_m value. Substrate concentration was determined by using the extinction coefficients 5438 M^{-1} cm^{-1} at 336 nm (Edans) and 15,100 M^{-1} cm^{-1} at 472 nm (Dabcyl). The initial rate, within 10% of the substrate consumption, was used to calculate the kinetic parameters using Michaelis-Menten equation fitting with the KaleidaGraph computer program (Synergy Software).

Enzyme Inhibition Assay—For inhibition constant measurements of CVB3 3C^{pro}, reactions were performed with 0.5 μM protease and 10 μM fluorogenic peptide in a buffer of 10 mM MES, pH 6.5, and 25 °C. The fluorescence change resulting from the reaction was followed with time using a 96-well fluorescence plate reader. To determine the inhibitory effect of various compounds, the compound and the enzyme were preincubated at 25 °C for 20 min prior to the addition of the substrate. The inhibition constant of SARS 3CL^{pro} was analyzed with reverse-phase HPLC using a C-18 column. K_i was calculated as described previously (18, 20).

Crystallization—All inhibitors, including TG-0204998, TG-0205486, and zinc *N*-ethyl-*N*-phenyldithiocarbamate (EPDTC), were dissolved in DMSO. Using the sitting-drop vapor diffusion method, the enzyme solution was mixed with inhibitor solutions at a molar ratio of 1:5 for 20 min before being combined with equal amounts of reservoir. 3CL^{pro}-EPDTC crystal of CoV-229E was obtained using a reservoir of 18% PEG 6000, 10% DMSO, 14% methyl-2,4-pentanediol (MPD), and 0.12 M

Downloaded from www.jbc.org at National Taiwan Univ Medical Library on June 10, 2009

TABLE 1
Data collection and refinement statistics for CVB3 $3C^{pro}$, SARS-CoV $3CL^{pro}$, and CoV-229E $3CL^{pro}$ crystals

	CV (Form I)	CV (C147A)	CV (Form II)	CV/EPDTC	CV/TG-0204998	SARS/TG-0204998	SARS/TG-0205486	229E/EPDTC
Data collection statistics								
Beamline	MicroMax002	NSRRC, BL13B1	PF, NW12	PF, BL6A	Spring-8, BL12B2	PF, BL5	NSRRC, BL17B2	PF, BL6A
Space group	$P2_1$	$P2_1$	$C2$	$C2$	$C2$	$C2$	$C2$	$P2_1$
Unite cell dimensions (Å, °)	38.9, 64.5, 68.3, β=90.6	39.0, 64.7, 68.7, β=91.2	75.8, 64.4, 40.3, β=115.7	76.4, 64.7, 39.2, β=115.6	76.8, 64.6, 39.5, β=115.9	108.6, 81.4, 53.2, β=104.6	108.7, 81.3, 53.3, β=104.5	53.5, 76.8, 76.7, β=91.0
NP[a]	2	2	1	1	1	1	1	2
Resolution range (Å)	30-2.0 (2.07-2.0)[b]	30-1.38 (1.43-1.38)	30-1.72 (1.78-1.72)	50-1.72 (1.78-1.72)	50-1.75 (1.81-1.75)	50-1.93 (2.00-1.93)	50-1.65 (1.77-1.65)	50-1.80 (1.86-1.80)
Unique observations	22,339 (1,816)	69,121 (6,740)	17,969 (1,511)	18,549 (1,830)	17,369 (1,718)	31,992 (2,841)	51,828 (4,986)	57,142 (5,551)
Redundancy	3.1 (1.8)	3.3 (2.7)	7.1 (5.8)	4.1 (3.6)	4.7 (4.3)	7.0 (5.4)	2.1 (2.1)	4.0 (3.7)
Completeness (%)	97.3 (79.5)	99.1 (96.8)	96.1 (81.6)	99.6 (99.0)	98.5 (97.8)	95.1 (85.3)	95.9 (93.3)	99.6 (97.0)
R_{merge} (%)	8.7 (31.1)	6.3 (57.8)	4.0 (30.0)	5.9 (38.7)	4.1 (47.9)	6.4 (33.3)	4.7 (36.9)	8.2 (38.8)
$I/\sigma(I)$	10.3 (2.7)	19.9 (2.1)	44.7 (3.7)	21.4 (3.1)	25.6 (2.0)	22.9 (4.8)	16.6 (2.1)	17.3 (2.9)
Refinement statistics								
Number of reflections (work/test)	19,954/1,014	59,601/3,177	16,617/842	15,742/815	15,473/793	29,429/1,527	46,161/2,448	47,499/2,538
R / R_{free} (%)	16.6/23.7	16.6/20.0	23.6/26.9	19.7/24.9	19.2/21.9	23.6/26.4	18.3/20.8	18.7/22.3
r.m.s deviation from ideal geometry								
Bonds (Å)	0.017	0.019	0.018	0.018	0.018	0.018	0.019	0.005
Angles (°)	1.89	1.92	2.01	2.07	2.19	1.98	1.97	1.31
Ramachandran plot								
Most favored (%)	88.1	88.1	83.6	86.1	86.8	87.5	92.5	90.1
Additional allowed (%)	10.9	11.3	14.4	11.9	11.9	10.6	6.4	9.7
Other regions (%)	1.0	0.7	2.1	1.3	1.3	1.9	1.2	0.2
Number of non-hydrogen atoms (average B-value, $Å^2$)								
Protein	2,798 (16.1)	2,796 (14.5)	1,371 (41.3)	1,399 (29.6)	1,399 (31.1)	2,371 (51.9)	2,371 (24.0)	4,620 (24.8)
Inhibitor				3 (43.9)	44 (58.9)	44 (50.9)	45 (22.5)	6 (29.4)
MPD								8 (24.3)
Water	380 (32.5)	624 (34.5)	234 (34.5)	208 (46.5)	199 (52.0)	173 (59.9)	460 (39.8)	469 (38.2)
PDB ID code	2ZTZ	2ZU1	2ZTY	2ZTX	2ZU3	2ZU4	2ZU5	2ZU2

[a] Number of protein molecules per asymmetric unit.
[b] Numbers in parentheses are for the outermost resolution shell.

Tris-HCl, pH 8.5. The crystals were flash-frozen with 20–25% ethylene glycol (v/v) as a cryoprotectant. For CVB3 $3C^{pro}$ and $3C^{pro}$-EPDTC crystals, a solution of 24% PEG 4000 and 0.1 M Tris-HCl, pH 8.0, was used as the reservoir. Native CVB3 $3C^{pro}$ was crystallized using 25% PEG 4000, 0.2 M $MgCl_2$, and 0.1 M Tris-HCl, pH 8.5, to give two monoclinic forms with space groups $P2_1$ (form I) and $C2$ (form II). The second crystal form was obtained when the enzyme solution was mixed with the reservoir at a volume ratio of 3:2. The other two CVB3 $3C^{pro}$ crystals, the TG-0204998 complex and the inactive C147A mutant, were obtained using a reservoir solution of 24–30% PEG 4000, 0.2 M $MgCl_2$, and 0.1 M Tris-HCl, pH 7.5–8.5. These crystals were rinsed with 26% glycerol as a cryoprotectant prior to data collection. Crystals of SARS $3CL^{pro}$ complexed with TG-0204998 and TG-0205486 were obtained using a reservoir solution of 3–6% PEG 6000, 4–6% DMSO or MPD, 1 mM dithiothreitol, 0.1 M MES, pH 6.5, and a cryoprotectant of 25–30% glycerol or ethylene glycol. All diffraction data were collected at cryogenic temperatures and processed and scaled using the program HKL2000 (22).

Structure Determination—All crystal structures were determined by molecular replacement using the program AMoRe (23). Using the SWISS-MODEL server (24) and the human RV $3C^{pro}$ (1CQQ; 4) structure as a template, a CV3B $3C^{pro}$ model was generated to solve its EPDTC complex structure. The remaining CV $3C^{pro}$ crystal structures were solved using the partially refined $3C^{pro}$-EPDTC complex structure as a search model. For SARS $3CL^{pro}$ and CoV-229E $3CL^{pro}$ complex structures, 1Z1I (25) and 1P9S (26) were used as the search models for molecular replacement, respectively.

The program CNS (Crystallography and NMR System) (27) was used for structure refinement. All manual modifications of the models were performed using the program XtalView (28). Difference Fourier ($F_o - F_c$) maps were calculated to locate the inhibitors and solvent molecules. Data collection and final model statistics are shown in Table 1. The atomic coordinates and structure factors of the various structures have been deposited in the Protein Data Bank (see Table 1).

Detection of Coxsackievirus B3 by RT-PCR—The confluent human embryonal rhabdomyosarcoma cells in 12-well plates were infected or mock-infected by coxsackievirus B3 at a multiplicity of infection of 0.01, with treatment of compound TG-0204998 at 0, 0.5, 1, 2, and 3 μM or compound TG-0205221 at 0, 1, 2, 5, 10, and 50 μM. Forty-eight hours after infection, total culture supernatants were harvested from the culture medium, and the supernatants of cell platelets were disrupted by freeze-thaw method. Viral RNA, extracted from 150 μl of total culture supernatant using the viral RNA extraction miniprep system kit (Viogene, Sunnyvale, CA) with the protocol recommended by the manufacturer, was eluted in 50 μl of diethylpyrocarbonate-treated water. RT-PCR amplifications were performed using a Reverse iT™ one-step RT-PCR kit

Downloaded from www.jbc.org at National Taiwan Univ Medical Library on June 10, 2009

(Abgene, Epsom, Surrey, UK) using the primer set specific for pan-enterovirus detection (29). RT-PCR was carried out in a 25-μl reaction mixture containing 11 μl of RNA template, 0.5 μl of 10 μM forward and reverse primers, 0.5 μl of kit-supplied enzyme mixture, and 12.5 μl of 2× RT-PCR Master Mix. The RT step included incubation at 42 °C for 1 h and then at 95 °C for 5 min followed by 25 cycles of 95 °C for 30 s, 50 °C for 30 s, and 72 °C for 1 min and a final elongation step of 72 °C for 5 min. PCR products were analyzed by gel electrophoresis on 1% agarose gel containing 2 μg/ml ethidium bromide. The DNA bands were visualized and photographed through UV transillumination.

RESULTS

Substrate Specificity and Kinetics of CVB3 3C^{pro}—The peptides corresponding to the autoprocessing sites of CVB3 3C^{pro} included LAGHQ↓GLPTM between vp2 and vp3, QNFFQ↓GPVED between vp3 and vp1, DAMEQ↓GVKDY between P2A and P2B, MAERQ↓NNSWL between P2B and P2C, EALFQ↓GPPVY between P2C and P3A, FAGFQ↓GAYTG between P3A and VPg, QAKVQ↓GPAFE between VPg and 3C, FNDEQ↓GEIEF between 3C and RNA-dependent RNA polymerase, and SAVLQ↓SGFRK derived from the N-terminal autoprocessing site of 3CL^{pro} from SARS-CoV (almost all of which contained a Gln followed by a small amino acid (Gly or Ser) to serve as the cleavage site) were tested as substrates for the protease (↓ indicates the cleavage site). Surprisingly, CVB3 3C^{pro} showed substantially better activity (30-fold) against SAVLQ↓SGFRK, the substrate of SARS-CoV 3CL^{pro}, than its own cleavage sites based on the HPLC assay (Fig. 1*A*). Therefore, the peptide Dabcyl-KTSAVLQSGFRKME-Edans, with the fluorescence quenching pair Dabcyl-Edans, was chosen for CVB3 protease activity assay by monitoring the fluorescence increase due to peptide bond cleavage in real time. The k_{cat} ($V_{max}/[E]$) and K_m values of the protease using this fluorogenic substrate were determined to be 6.2 × 10^{-3} s^{-1} and 9.2 ± 1.7 μM, respectively (Fig. 1*B*).

Evaluation of Inhibitors—Because CVB3 3C^{pro} showed substrate specificity similar to that of SARS-CoV 3CL^{pro}, our reported 3CL^{pro} inhibitors were tested against the recombinant 3C^{pro} of CVB3 by using the fluorogenic substrate to determine their inhibitory activities. EPDTC, which inhibited SARS protease with a K_i of 1 μM (19), showed lower inhibition against CVB3 3C^{pro} (K_i = 4.4 ± 0.7 μM) (Fig. S1). From the inhibition pattern, it was shown to be competitive with respect to the substrate. For the peptidomimetic inhibitors, the K_i values of TG-0203770, TG-0204998, TG-0205221, and TG-0205486 against SARS-CoV 3CL^{pro} were 0.058, 0.038, 0.054, and 0.099 μM, respectively. The K_i values of TG-0203770 and TG-0205221 are reported elsewhere (20). Larger K_i values of 1.5, 0.8, 2.5, and 0.4 μM for the four compounds against CVB3 3C^{pro} were observed, indicating their lower affinity toward CVB3 3C^{pro} (Table 2). TG-0204998 and TG-0205486 have similar structures, differing only by an extra cyclopropyl group at the P1′ residue, and they also possess similar potency with a K_i of 0.8 and 0.4 μM, respectively, against CVB3 3C^{pro}.

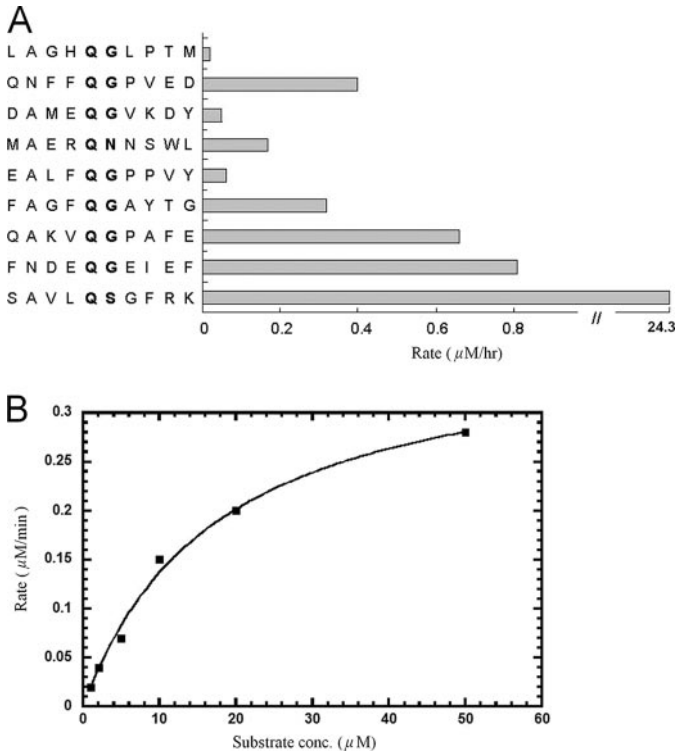

FIGURE 1. **Substrate specificity and kinetics of CVB3 3C^{pro}.** *A*, compared with the peptides derived from its processing sites, CVB3 3C^{pro} showed the best activity toward the preferred substrate, SAVLQSGFRK, of SARS-CoV 3CL^{pro}. *B*, by using the fluorogenic substrate Dabcyl-KTSAVLQSGFRKME-Edans, the initial reaction rates of the protease under a variety of different substrate concentrations were plotted against substrate concentrations to obtain the V_{max} and K_m values of the enzyme. The kinetic data were fitted with the Michaelis-Menten equation and k_{cat} ($V_{max}/[E]$) and K_m were determined to be 6.2 × 10^{-3} s^{-1} and 9.2 ± 1.7 μM, respectively.

Structures of CVB3 3C^{pro} and CoV 3CL^{pro}—Two crystal forms belonging to the monoclinic space groups $P2_1$ (form I) and $C2$ (form II), of CVB3 3C protease were obtained under similar crystallization conditions (Table 1). Form I crystal has two molecules per asymmetric unit related by a pseudo-dyad; form II crystal has only one molecule. As shown in Fig. 2*A*, the structure of CVB3 3C^{pro} adopts a chymotrypsin protein fold similar to those of RV 3C^{pro} (4) and other viral 3C proteases. The root-mean-square deviation between CVB3 3C^{pro} and RV 3C^{pro} is 0.73 Å for 166 Cα atoms. The N terminus starts with an α-helix of residues 1–14 and is followed by two topologically equivalent β-barrel domains comprising residues 15–77 and 99–173, which pack together to form an extended shallow groove for substrate binding. The catalytic triad of Cys^{147}, His^{40}, and Glu^{71} is located in the cleft between the two β-barrel domains. The protease structures in the two crystal forms are very similar, except that the loop of residues 143–146 is disordered, the side chain of Cys^{147} has a different orientation, and His^{40} is slightly shifted in the form II crystal (Fig. 2*A*). This loop is flexible on the protein surface, which may regulate the substrate binding. Such variable loop conformation was also observed in the 3C^{pro} structure of foot-and-mouth disease virus (30). The C147A mutant of CVB3 3C^{pro} crystallized in a unit cell similar to that of the wild-type form I crystal and diffracted to 1.38 Å (Table 1 and Fig. S2). Both complexes of CVB3 3C^{pro} with EPDTC and TG-0204998 crystallized in the form II unit

Downloaded from www.jbc.org at National Taiwan Univ Medical Library on June 10, 2009

TABLE 2
Peptidomimetic inhibitors against CVB3 3C^{pro} and SARS-CoV 3CL^{pro} (Ref. 22)

Compounds		K_i (μM) for *in vitro* inhibition	
		CVB3 3C^{pro}	SARS-CoV 3CL^{pro}
TG-0203770	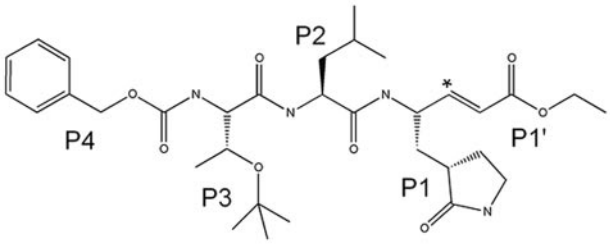	1.5[a]	0.058[b]
TG-0204998	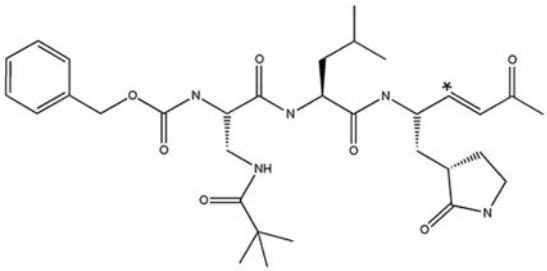	0.8	0.038
TG-0205221	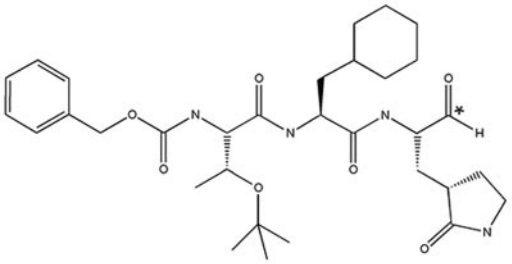	2.5	0.054
TG-0205486	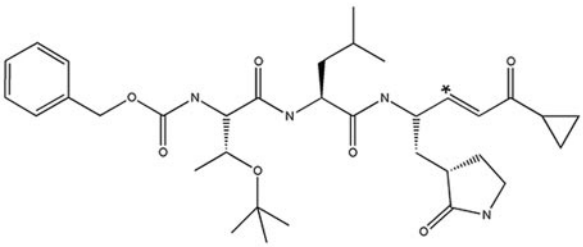	0.4	0.099

* Michael addition site.
[a] Analyzed using fluorescence.
[b] Analyzed using reverse-phase HPLC.

cell, with only a slight variation in the protein conformation (Fig. 2*A*).

The complex crystals of SARS-CoV 3CL^{pro}/TG-0204998 and 3CL^{pro}/TG-0205486 belong to the *C*2 space group with one complex model per asymmetric unit (Table 1). In these structures, the inhibitors were well defined in the Fourier maps. CoV-229E 3CL^{pro}-EPDTC complex crystallized in a $P2_1$ unit cell with a dimer as its asymmetric unit (Fig. 2*B*). As reported previously, both CoV-229E and SARS-CoV 3CL^{pro} are homodimers with three domains in each monomer. The catalytic dyad of His-Cys is located in the active site in the cleft between domains I and II, whereas domain III participates in the protease dimerization (26, 31). In contrast, CVB3 3C^{pro} is a monomer, and it does not contain the dimerization domain III. By employing the program O (32), CVB3 3C^{pro} monomer can be superimposed onto SARS 3CL^{pro} with a root-mean-square deviation of 2.11 Å for 121 matched Cα atoms or 1.06 Å for 48 Cα if more stringent criteria were used. His^{40} and Cys^{147} in the catalytic triad of CVB3 3C^{pro} coincide almost perfectly with the His-Cys dyads of the CoV proteases (Fig. 2*C*). Although the two types of proteases share very little sequence homology, structure-based sequence comparison reveals some similarity in the regions of domains I and II (Fig. 2*D*), which explains the similar substrate specificity and catalytic mechanism. However, the different affinities of the protein for the inhibitors encouraged further analysis of their interactions.

Downloaded from www.jbc.org at National Taiwan Univ Medical Library on June 10, 2009

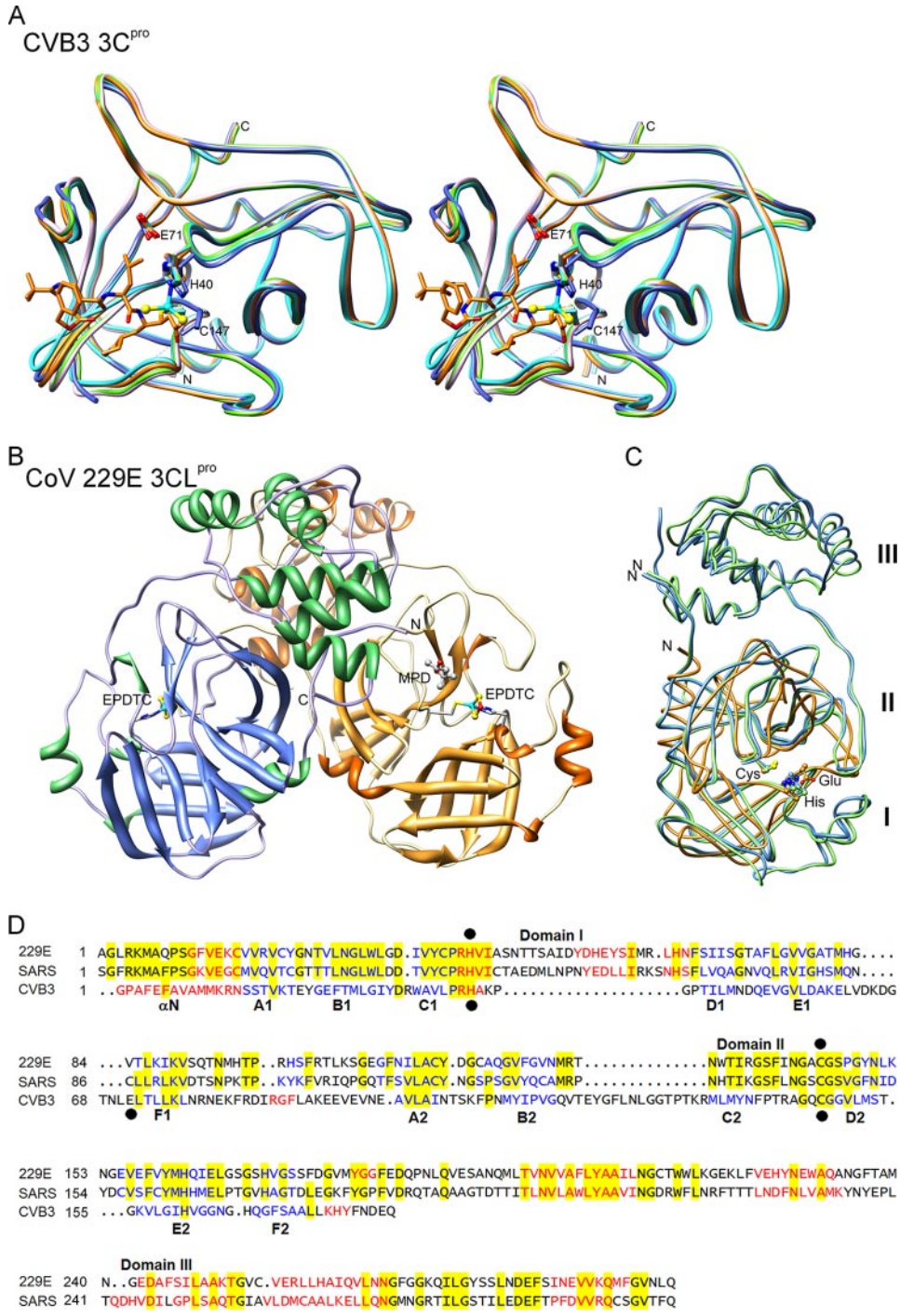

FIGURE 2. **Comparison of 3C^{pro} and 3CL^{pro} structures.** *A*, stereo view of five CVB3 3C^{pro} structures (form I, form II, C147A, and complexed with EPDTC and TG-0204998) superimposed and colored in *pink*, *marine*, *green*, *cyan*, and *orange*, respectively. EPDTC, TG-0204998, and the catalytic residues are shown as *sticks*, and the triad catalytic residues His^{40}, Glu^{71}, and Cys^{147} are labeled. The disordered residues 143–146 in the form II crystal are indicated by *dashed lines*. *B*, overall three-dimensional structure of CoV-229E 3CL^{pro} with bound EPDTC and MPD, colored by secondary structure elements. *C*, crystal structures of CVB3 3C^{pro}, SARS-CoV 3CL^{pro} (Protein Data Bank code 2Z9J), and CoV-229E 3CL^{pro} are superimposed and colored in *orange*, *light blue*, and *green*, respectively. Their catalytic residues are indicated. The labels *I*, *II*, and *III* (on the *right*) denote the three domains of 3CL^{pro}. *D*, structure-based sequence alignment of CoV-229E 3CL^{pro}, SARS-CoV 3CL^{pro}, and CVB3 3C^{pro}. Residues of α-helices are shown in *red* and those of β-strands in *blue*, and the identical residues are highlighted in *yellow*. Catalytic residues are marked with *black dots*. The three domains according to the 3CL^{pro} structures are shown *above* the sequence, and the secondary structure elements of CVB3 3C^{pro} are shown *below*.

Interactions of 3C^{pro} and 3CL^{pro} with the Inhibitors—The structure of EPDTC is shown in Fig. 3*A*, and those of the peptide inhibitors are shown in Table 1. The local structures of CVB3 3C^{pro} and CoV-229E 3CL^{pro} in complex with EPDTC are shown in Fig. 3, *B* and *C*, and the previously determined structure of SARS-CoV 3CL^{pro} in complex with EPDTC is shown in Fig. 3*D* for comparison. The environments of the peptide inhibitors bound to the proteases are shown in Fig. 4. Omit maps for the bound inhibitors are shown in Fig. 5.

The zinc sites were confirmed by anomalous difference Fourier maps (not shown). The binding mode of EPDTC in the CVB3 and CoV-229E proteases are similar to that observed in SARS-CoV 3CL^{pro}, where the Zn^{2+} binds to the two catalytic residues Cys and His. The zinc and two sulfur atoms of EPDTC were clearly seen in every subunit, but the bulky substituent groups in both crystals were invisible. In the zinc center, the S—Zn—S bond angle is 103.1° for CVB3 3C^{pro}, similar to the 107.2° observed in SARS-CoV 3CL^{pro} structure; but a distorted tetrahedral geometry was observed for CoV-229E 3CL^{pro} (Fig. 5*B*), with an S—Zn—S angle of 85.25°, despite the restraints to an ideal angle of 109.5° employed in the refinement.

In addition to Zn^{2+}, an MPD molecule from the crystallization reservoir was found in one subunit of CoV-229E 3CL^{pro}, which is located in the S1 pocket. The two oxygen atoms of MPD form two H-bonds with the side chain of His^{162} and Gln^{141} with distances of 2.66 and 3.15 Å, respectively. MPD binds in a similar position to that of DMSO (coming from the solvent to dissolve the inhibitor) in SARS-CoV 3CL^{pro} complexed structure. No such organic molecule was observed in the complex structure of CVB3 3C^{pro} with EPDTC.

In the CVB3 3C^{pro}/TG-0204998 structure (Fig. 4*A*), the α,β-unsaturated ethyl ester occupies the S1′ site, which is in close proximity to the catalytic center. The Michael acceptor forms a covalent C–S bond with the Cys^{147}. The lactam ring occupies the S1 site, as it is a Gln mimic and forms two H-bonds with Thr^{142} and His^{161}. The P2 Leu side chain occupies the S2 site, a large hydrophobic pocket.

Downloaded from www.jbc.org at National Taiwan Univ Medical Library on June 10, 2009

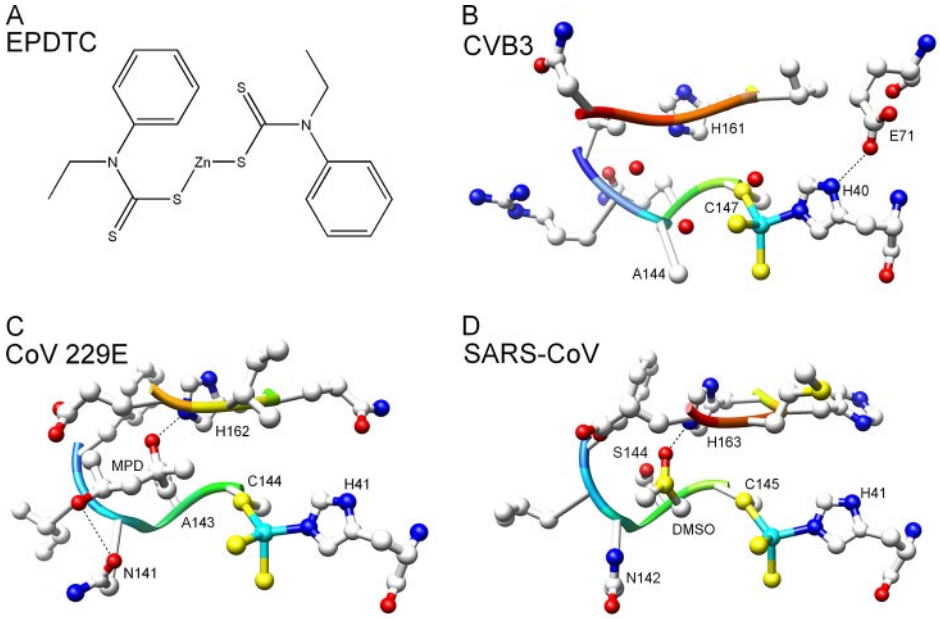

FIGURE 3. **EPDTC bound to the three different proteases.** *A*, schematic drawing of the chemical structure of zinc-coordinating inhibitor EPDTC. *B–D*, the inhibitor is coordinated to the catalytic dyad residues His and Cys of CVB3 3C^{pro}, CoV-229E 3CL^{pro}, and SARS-CoV 3CL^{pro} with a zinc-centered tetrahedral geometry. A MPD molecule located in the S1 pocket of CoV-229E 3CL^{pro} and a DMSO molecule in SARS-CoV 3CL^{pro} are shown in addition to the inhibitor. The oxygen atoms are shown in *red*, nitrogen in *blue*, sulfur in *orange*, and carbon in *gray*. The zinc ions are depicted as a *cyan sphere*.

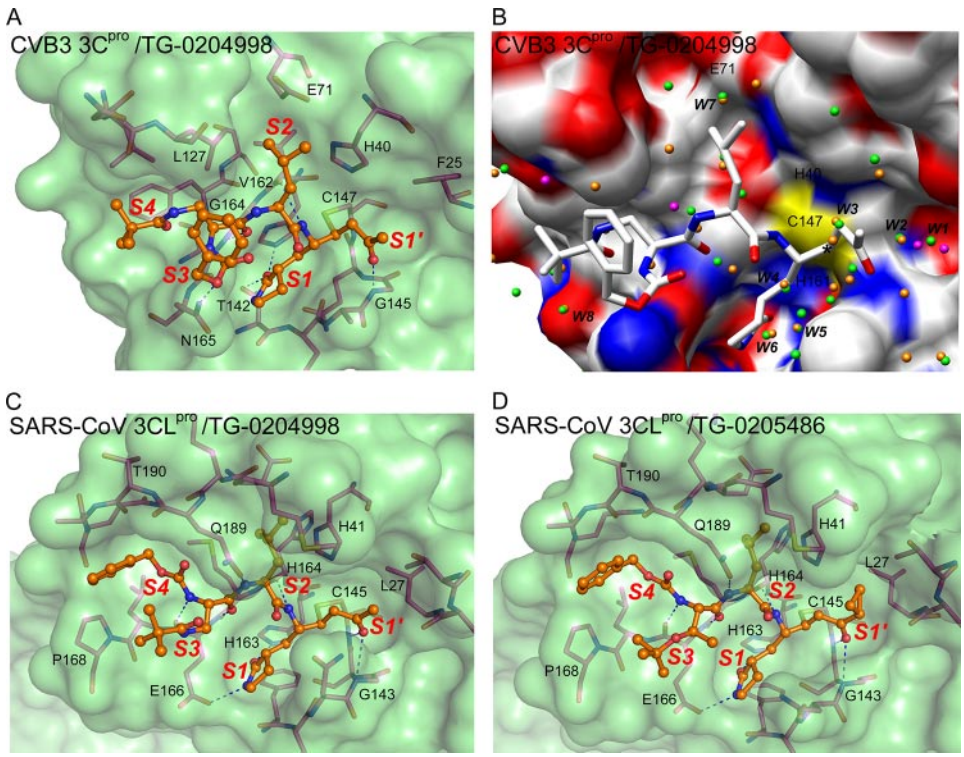

FIGURE 4. **Peptidomimetic inhibitors bound to the proteases.** *A*, the active site of CVB3 3C^{pro} with the bound TG-0204998. Protein is rendered as a semitransparent solvent-accessible surface with associated protein backbone and side chain atoms. The oxygen atoms are shown in *red*, nitrogen in *blue*, sulfur in *yellow*, and protein carbon atoms in *magenta*. The inhibitor atoms are shown as *ball-and-stick* form and colored in *orange* for carbon. The sulfur atom of Cys^{147} is covalently attached to the inhibitor carbon. The substrate binding subsites are designated as S1′, S1, S2, S3, and S4. *B*, conserved water molecules, identified by superimposing the two molecules of CVB3 3C^{pro} C147A mutant on the TG-0204998 complex of CVB3 3C^{pro}. The water molecules are shown here as *spheres* colored *green*/*orange* (C147A) and *magenta* (complex). The protein model of the TG-0204998 complex structure is shown as an electrostatic surface and TG-0204998 as *sticks*. The conserved water molecules of the C147A mutant structure in the active site are marked. The *black star* indicates the Michael addition site. *C* and *D*, the active site of SARS 3CL^{pro} with bound TG-0204998 (*C*) and TG-0205486 (*D*), colored as in *A*. The substrate-binding subsites are also indicated.

Interestingly, the P3 group of TG-0204998 is actually located in the S4 site. The P4 benzoxy ester group lacks strong electron densities (Fig. 5*C*) because it is exposed to the bulk solvent. In Fig. 4*B*, two protein molecules in the C147A structure are superimposed, along with the TG-0204998 complex and eight conserved water molecules with distances of less than 0.4 Å between the equivalents. Some of these waters occupied the inhibitor binding sites, whereas others may help improve the drug-protein interactions (see below).

In the SARS-CoV 3CL^{pro}/TG-0204998 structure (Fig. 4*C*), Cys^{145} attacks the α-carbon of the α,β-unsaturated ketone at the P1′ position to form a covalent C–S bond of 1.99 Å and induces hydrogen bonding between the ketone oxygen and the N-H groups of Gly^{143} and Cys^{145} itself in the S1′ pocket. In the S1 site, the carbonyl oxygen and the nitrogen of the five-member lactam ring at the P1 position form hydrogen bonds with His^{163} and Glu^{166}, respectively. The following P2 Leu side chain binds into a hydrophobic S2 pocket. The P3 group is directed toward the bulk solvent. The benzoxy group at the P4 position is bound in the S4 pocket with its phenyl ring aligned parallel to a flat surface near Ala^{191}. Most of the carbon atoms (4 of 6) in the phenyl ring show hydrophobic contacts with the protein.

In the structure of SARS-CoV 3CL^{pro}/TG-0205486 (Fig. 4*D*), the inhibitor adopts a similar binding mode to that in the above structure. In both structures, the peptide N-H groups of residues P1 to P3 form four hydrogen bonds with the backbone CO groups of His^{164} and Glu^{166}, and the side chain of Gln^{189}. In addition, the CO group of P3 interacts with the N-H groups of Glu^{166}.

Antiviral Compounds TG-0204998 and TG-0205221 Can Effectively Inhibit Replication of CVB3—The critical and essential step in coxsackievirus replication is polyprotein cleavage by 3C^{pro} after viral

Downloaded from www.jbc.org at National Taiwan Univ Medical Library on June 10, 2009

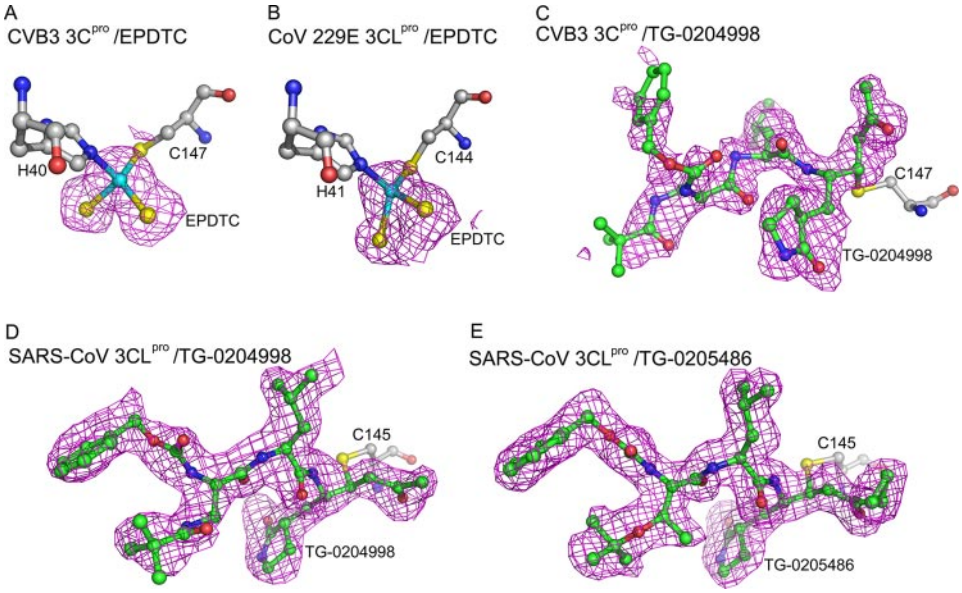

FIGURE 5. **Omit maps of inhibitors.** $F_o - F_c$ omit maps (*magenta*) were calculated for the five inhibitors and contoured at the 2.0 σ level. The inhibitor and inhibitor-binding residues are shown as *ball-and-stick* models with carbon atoms in *green* and *gray*. The sulfur, nitrogen, and oxygen atoms are colored in *yellow*, *blue*, and *red*, respectively. *A* and *B*, EPDTC bound to CVB3 3C^{pro} and CoV-229E 3CL^{pro}. The zinc ion (*cyan sphere*) of EPDTC was coordinated to the Cys and His residues. *C* and *D*, TG-0204998 in covalent bond with the Cys of CVB3 3C^{pro} and SARS-CoV 3CL^{pro}. *E*, TG-0205486 in covalent bond with the Cys of SARS-CoV 3CL^{pro}.

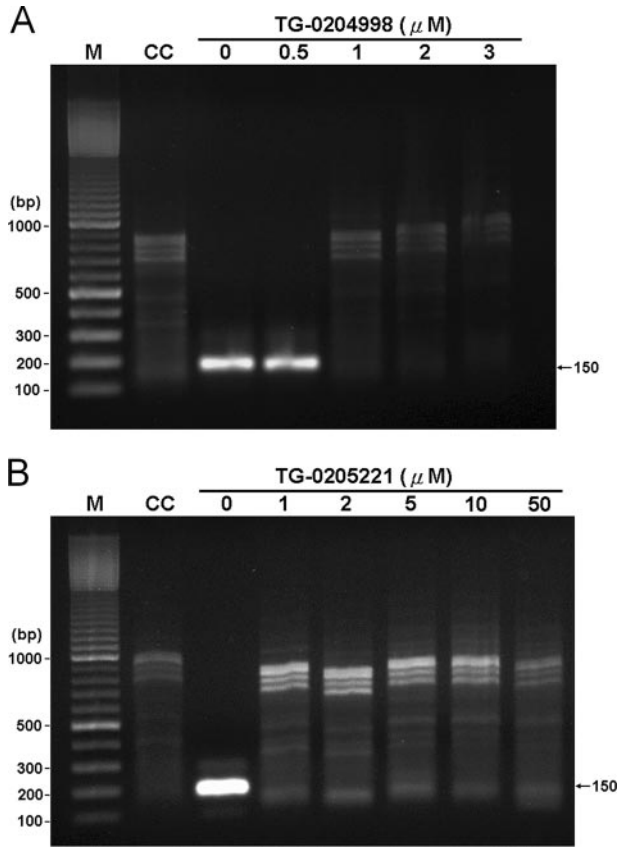

FIGURE 6. **CVB3 replication in rhabdomyosarcoma cells detected by RT-PCR.** RNAs extracted from mock-infected (*CC*, *lane 2*) or CVB3-infected rhabdomyosarcoma cells in the presence of compound TG-0204998 at 0, 0.5, 1, 2, and 3 μM (*A*, *lanes 3–7*) or compound TG-0205221 at 0, 1, 2, 5, 10 and 50 μM (*B*, *lanes 3–8*) were amplified by RT-PCR as described under "Experimental Procedures" and resolved in 1% agarose gel. The expected size (150 bp) of the RT-PCR product is indicated with an *arrow*. The 100-bp DNA marker shows the molecular size (*M*, *lane 1*).

protein translation, which is the potential target for antiviral drugs TG-0204998 and TG-0205221 (33). To observe the effect of compounds TG-0204998 and TG-0205221 on virus replication, RT-PCR was applied to detect the coxsackievirus genome in the infected cells. As shown in Fig. 6, a 150-bp DNA fragment could be detected in virus-infected cells either in the absence or presence of 0.5 μM TG-0204998. However, no specific DNA fragment could be found when the concentration of compound TG-0204998 or TG-0205221 was increased to 1 μM, indicating that both compounds could effectively block viral replication in the host cells.

DISCUSSION

Two kinds of proteases, 3C^{pro} and 3CL^{pro}, serve as drug targets for developing inhibitors against picornaviruses and coronaviruses, respectively. Although these two proteases do not share sequence homology, they share similar substrate specificity in recognizing Gln as the P1 residue, a hydrophobic residue at the P2 position, and a small amino acid residue at the P1′ position. In this study, we found that CVB3 3C^{pro} actually prefers the substrate of SARS-CoV 3CL^{pro} derived from its N-terminal processing site. However, the inhibitors could not inhibit both proteases equally (Table 2), suggesting some structural differences in the active site. To understand the structural basis of the specificity, we solved the structures of 3C^{pro} from CVB3 and 3CL^{pro} from CoV-229E and SARS-CoV with the same inhibitors to compare their binding modes. The information obtained here is useful for designing specific inhibitors against each kind of the proteases.

For the zinc-coordinating inhibitor EPDTC, similar to the previously determined binding mode in the structure of a complex with SARS-CoV 3CL^{pro}, the Zn^{2+} cation is tetrahedrally coordinated by the His-Cys catalytic residues of CVB3 3C^{pro} (Fig. 3*B*). The binding is facilitated by the suitable distances from the nitrogen atom of His and the S^- anion of Cys to the zinc center in both 3C and 3CL proteases. However, the EPDTC inhibition of CVB3 3C^{pro} is 4.4-fold weaker (Fig. S1); this is probably because the side chain of Glu^{71} is hydrogen-bonded to the Nδ1 atom of His^{40} to favor the protonation of Nϵ2. Therefore the Nϵ2 atom must be deprotonated before EPDTC binding takes place. The lack of electron density for the bulky substituent groups might suggest that they are disordered. According to a computer model of the inhibitor with SARS-CoV 3CL^{pro} (21), the entire EPDTC could be accommodated in the active site with sufficient room for the bulky side groups to rotate about. On the other hand, a molecule of DMSO (SARS-CoV) or MPD (CoV-229E) is bound in the S1 site of 3CL^{pro}. Although the DMSO molecule forms a hydrogen bond with

Downloaded from www.jbc.org at National Taiwan Univ Medical Library on June 10, 2009

Ser[144] of the former enzyme, the smaller side chain of Ala[143] in the latter case provides hydrophobic interaction and larger space for MPD bonding (Fig. 3, *C* and *D*). No such solvent molecule was seen in the complex structure of CVB3 3C^{pro} with EPDTC, because its more open S1 pocket fails to trap small molecules.

Unlike 3CL^{pro}, which is dimeric and in which each subunit is composed of three domains, 3C^{pro} is a monomer with only the two catalytic domains. Structure-based sequence alignment shows that 3CL^{pro} has a large loop between β-strands C1 and D1, whereas 3C^{pro} has smaller loops inserted between E1 and F1 and between B2 and C2 (Fig. 2*D*). The C1–D1 loop of SARS-CoV 3CL^{pro} secures the S2 hydrophobic pocket for the P2 side chain. The two loops E1–F1 and B2–C2 of CVB3 3C^{pro} are also adjacent to the active site, and they modulate the binding of the P3 and P4 residues. The four peptidomimetic compounds have a higher K_i for CVB3 3C^{pro} than for SARS-CoV 3CL^{pro} in general, not only because it has a more open active site but also because the binding sites are different.

For the peptidomimetic inhibitors, both TG-0204998 and TG-0205486 bind to the active site of SARS-CoV 3CL^{pro} in similar modes, whereas TG-0204998 binds differently to CVB3 3C^{pro}. The P2 cyclohexyl side chain of TG0205221 fits well in the S2 site of SARS-CoV 3CL^{pro} but is too bulky for CVB3 3C^{pro}, whereas the P2 Leu of TG0204998 fits well in both. The E1–F1 loop of CVB3 3C^{pro} makes the S2 site shallow and open (Fig. 4*B*), which is consistent with its 46-fold higher K_i of TG-0205221 (Table 2). On the other hand, our CVB3 3C^{pro} structure is analogous to that of RV 3C^{pro}, and a P2 phenyl side chain may be preferred by CVB3 3C^{pro} as evidenced by the tight binding of AG7088 to RV 3C^{pro} (4). Moreover, the *t*-butyl group of P3 is favored for tight binding to the S3 site of SARS-CoV 3CL^{pro}, which enhances the inhibition by more than 10-fold (20). Conversely, the P3 Val in AG7088 fits RV 3C^{pro} very well, but the additional *t*-butyl group makes our compounds weaker inhibitors of CVB3 3C^{pro}. With the *t*-butyl group, the bulky P3 residue is actually relocated to the hydrophobic environment in the S4 site formed by the B2–C2 loop of CVB3 3C^{pro}, leaving the unbound P4 benzoxy group facing the bulk solvent (Figs. 2*A* and 4*B*). This may also contribute to the higher K_i. Removal of the P3 *t*-butyl group or the entire P4 residue may improve the inhibitors against CVB3 3C^{pro}.

In these inhibitors, the P1 site favors Gln or its mimicking lactam ring, and the lactam ring provides 15-fold better inhibitory activity than Gln, as revealed by the previously reported structure-activity relationships (4). The strong binding of the lactam ring to the proteases is evidenced by the multiple hydrogen bond formations in the crystal structures (Fig. 4). The addition of a cyclopropyl group to the P1′ residue of TG-0205486 enhances the inhibition against CVB3 3C^{pro} by almost 4-fold as compared with TG-0203770, but it becomes weaker against SARS-CoV 3CL^{pro} (Table 2). As shown in Fig. 4*D*, the triangular group tends to clash with the protein atoms because of the more limited space of the S1′ site adjacent to loop C1–D1. In CVB3 3C^{pro}, the S1′ site is more open, yet still flanked by the hydrophobic side chain of Phe[25].

The conserved water molecules in the active site, as revealed by the high-resolution crystal structure of the C147A mutant of CVB3 3C^{pro} (Fig. 4*B*), may also offer some trends for optimizing the inhibitors. If the water model is superimposed on the bound TG-0204998 molecules, W3 and W4 are equivalent to two carbon atoms in the P1′ and P1 residues of TG-0204998. W5 and W6 are located in the S1 pocket, forming hydrogen bonds to the protein including His[161]. These are to be displaced by the P1 lactam ring with a similar bonding pattern. W7 is located in the S2 pocket with a distance of about 1.85 Å to the side chain carbon of P2 Leu and is hydrogen-bonded to the side chain of Glu[71] at a distance of 2.98 Å. Based on these observations, a new drug can have the W4-equivalent carbon atom replaced by a nitrogen or sulfur, but the W3-equivalent carbon cannot be changed because it is part of the α,β-unsaturated aldehyde for the Michael addition. The P2 Leu may be replaced by an Arg or a Lys residue, which can interact with Glu[71].

In summary, we have shown here that the antiviral compounds TG-0204998 and TG-0205221 inhibit the viral protease, thus preventing CVB3 genome replication. Our study reveals the key interactions in determining the binding specificity of the inhibitors against 3C and 3CL proteases. The information will be useful for further inhibitor optimization and drug discovery.

Acknowledgments—We are grateful to the National Synchrotron Radiation Research Center of Taiwan, SPring-8, and Photon Factory of Japan for beam time allocations. We also thank Chi-Shen Wu and Li-Wen Chang of TaiGen Biotechnology, Taipei, for kindly providing peptidomimetic inhibitor compounds.

REFERENCES

1. David, M. K., Peter, M. H., Diane, E. G., Robert, A. L., Malcolm, A. M., Bernard, R., and Stephen, E. S. (2007) *Fields Virology*, 5th Ed., pp. 795–893, Wolters Kluwer Health-Lippincott Williams and Wilkins, New York
2. Maze, S. S., and Adolph, R. J. (1990) *Clin. Cardiol.* **13,** 69–79
3. Porter, A. G. (1993) *J. Virol.* **67,** 6917–6921
4. Matthews, D. A., Dragovich, P. S., Webber, S. E., Fuhrman, S. A., Patick, A. K., Zalman, L. S., Hendrickson, T. F., Love, R. A., Prins, T. J., Marakovits, J. T., Zhou, R., Tikhe, J., Ford, C. E., Meador, J. W., Ferre, R. A., Brown, E. L., Binford, S. L., Brothers, M. A., DeLisle, D. M., and Worland, S. T. (1999) *Proc. Natl. Acad. Sci. U. S. A.* **96,** 11000–11007
5. Johnson, T. O., Hua, Y., Luu, H. T., Brown, E. L., Chan, F., Chu, S. S., Dragovich, P. S., Eastman, B. W., Ferre, R. A., Fuhrman, S. A., Hendrickson, T. F., Maldonado, F. C., Matthews, D. A., Meador, J. W., Patick, A. K., Reich, S. H., Skalitzky, D. J., Worland, S. T., Yang, M., and Zalman, L. S. (2002) *J. Med. Chem.* **45,** 2016–2023
6. Binford, S. L., Maldonado, F., Brothers, M. A., Weady, P. T., Zalman, L. S., Meador, J. W., Matthews, D. A., and Patick, A. K. (2005) *Antimicrob. Agents Chemother.* **49,** 619–626
7. Peiris, J. S., Lai, S. T., Poon, L. L., Guan, Y., Yam, L.Y., Lim, W., Nicholls, J., Yee, W. K., Yan, W. W., Cheung, M. T., Cheng, V. C., Chan, K. H., Tsang, D. N., Yung, R. W., Ng, T. K., and Yuen, K. Y. (2003) *Lancet* **361,** 1319–1325
8. Ksiazek, T. G., Erdman, D., Goldsmith, C. S., Zaki, S. R., Peret, T., Emery, S., Tong, S., Urbani, C., Comer, J. A., Lim, W., Rollin, P. E., Dowell, S. F., Ling, A. E., Humphrey, C. D., Shieh, W. J., Guarner, J., Paddock, C. D., Rota, P., Fields, B., DeRisi, J., Yang, J. Y., Cox, N., Hughes, J. M., LeDuc, J. W., Bellini, W. J., and Anderson, L. J. (2003) *N. Engl. J. Med.* **348,** 1953–1966
9. Fouchier, R. A., Kuiken, T., Schutten, M., van Amerongen, G., van Doornum, G. J., van den Hoogen, B. G., Peiris, M., Lim, W., Stohr, K., and Osterhaus, A. D. (2003) *Nature* **423,** 240
10. Drosten, C., Gunther, S., Preiser, W., van der Werf, S., Brodt, H. R., Becker, S., Rabenau, H., Panning, M., Kolesnikova, L., Fouchier, R. A., Berger, A.,

Downloaded from www.jbc.org at National Taiwan Univ Medical Library on June 10, 2009

Burguiere, A. M., Cinatl, J., Eickmann, M., Escriou, N., Grywna, K., Kramme, S., Manuguerra, J. C., Muller, S., Rickerts, V., Sturmer, M., Vieth, S., Klenk, H. D., Osterhaus, A. D., Schmitz, H., and Doerr, H. W. (2003) *N. Engl. J. Med.* **348,** 1967–1976
11. Bradburne, A. F., Bynoe, M. L., and Tyrrell, D. A. (1967) *Br. Med. J.* **3,** 767–769
12. Woo, P. C., Lau, S. K., Chu, C. M., Chan, K. H., Tsoi, H. W., Huang, Y., Wong, B. H., Poon, R. W., Cai, J. J., Luk, W. K., Poon, L. L., Wong, S. S., Guan, Y., Peiris, J. S., and Yuen, K. Y. (2005) *J. Virol.* **79,** 884–895
13. Van der Hoek, L., Pyrc, K., and Berkhout, B. (2006) *FEMS Microbiol. Rev.* **30,** 760–773
14. Fan, K., Wei, P., Feng, Q., Chen, S., Huang, C., Ma, L., Lai, B., Pei, J., Liu, Y., Chen, J., and Lai, L. (2004) *J. Biol. Chem.* **279,** 1637–1642
15. Shie, J. J., Fang, J. M., Kuo, T. H., Kuo, C. J., Liang, P. H., Huang, H. J., Wu, Y. T., Jan, J. T., Cheng, Y.-S. E., and Wong, C. H. (2005) *Bioorg. Med. Chem.* **13,** 5240–5252
16. Liang, P. H. (2006) *Curr. Top. Med. Chem.*, **6,** 361–376
17. Wang, H. M., and Liang, P. H. (2007) *Expert Opin. Ther. Pat.* **17,** 533–546
18. Hsu, J. T., Kuo, C. J., Hsieh, H. P., Wang, Y. C., Huang, K. K., Lin, C. P., Huang, P. F., Chen, X., and Liang, P. H. (2004) *FEBS Lett.* **574,** 116–120
19. Lee, C. C., Kuo, C. J., Hsu, M. F., Liang, P. H., Fang, J. M., Shie, J. J., and Wang, A. H.-J. (2007) *FEBS Lett.* **581,** 5454–5458
20. Yang, S., Chen, S. J., Hsu, M. F., Wu, J. D., Tseng, C. T., Liu, Y. F., Chen, H. C., Kuo, C. W., Chang, L. W., Chen, W. C., Lio, S. Y., Chang, T. Y., Hung, H. H., Shr, H. L., Liu, C. Y., Huang, Y. A., Chang, L. Y., Hsu, J. C., Peters, C. J., Wang, A. H.-J., and Hsu, M. C. (2006) *J. Med. Chem.* **49,** 4971–4980
21. Kuo, C. J., Chi, Y. H., Hsu, T. A., and Liang, P. H. (2004) *Biochem. Biophys. Res. Comm.* **318,** 862–867
22. Otwinowski, Z., and Minor, W. (1997) in *Processing of X-ray Diffraction Data Collected in Oscillation Mode* (Sweet, R. M., ed) pp. 307–326, Academic Press, New York
23. Navaza, J. (1994) *Acta Crystallogr. Sect. A* **50,** 157–163
24. Schwede, T., Kopp, J., Guex, N., and Peitsch, M. C. (2003) *Nucleic Acids Res.* **31,** 3381–3385
25. Hsu, M. F., Kuo, C. J., Chang, K. T., Chang, H. C., Chou, C. C., Ko, T. P., Shr, H. L., Chang, G. G., Wang, A. H.-J., and Liang, P. H. (2005) *J. Biol. Chem.* **280,** 31257–31266
26. Anand, K., Ziebuhr, J., Wadhwani, P., Mesters, J. R., and Hilgenfeld, R. (2003) *Science* **300,** 1763–1767
27. Brünger, A. T., Adams, P. D., Clore, G. M., Delano, W. L., Gros, P., Grosse-Kunstleve, R. W., Jiang, J. S., Kuszewski, J., Nilges, M., Pannu, N. S., Read, R. J., Rice, L. M., Simonson, T., and Warren, G. L. (1998) *Acta Crystallogr. Sect. D* **54,** 905–921
28. McRee, D. E. (1999) *J. Struct. Biol.* **125,** 156–165
29. Monpoeho, S., Dehee, A., Miqnotte, B., Schwartzbrod, L., Marechal, V., Nicolas, J. C., Billaudel, S., and Ferre, V. (2000) *BioTechniques* **29,** 88–93
30. Birtley, J. R., Knox, S. R., Jaulent, A. M., Brick, P., Leatherbarrow, R. J., and Curry, S. (2005) *J. Biol. Chem.* **280,** 11520–11527
31. Shi, J., Wei, Z., and Song, J. (2004) *J. Biol. Chem.* **279,** 24765–24773
32. Jones, T. A., Zou, J. Y., Cowan, S. W., and Kjeldgaard, M. (1991) *Acta Crystallogr. Sect. A* **47,** 392–400
33. Shih, S. R., Chiang, C., Chen, T. C., Wu, C. N., Hsu, J. T. A., Lee, J. C., Hwang, M. J., Li, M. L., Chen, G. W., and Ho, M. S. (2003) *J. Biomed. Sci.* **11,** 239–248

Downloaded from www.jbc.org at National Taiwan Univ Medical Library on June 10, 2009